# Investigating the Optical Properties of a Laser Induced 3D Self-Assembled Carbon–Metal Hybrid Structure

Butt, Muhammad Abdullah; Lesina, Antonino Calà; Neugebauer, Martin; Bauer, Thomas; Ramunno, Lora; Vaccari, Alessandro; Berini, Pierre; Petrov, Yuriy; Danilov, Denis; More Authors

**DOI**
10.1002/smll.201900512

**Publication date**
2019

**Document Version**
Accepted author manuscript

**Published in**
Small

**Citation (APA)**
Butt, M. A., Lesina, A. C., Neugebauer, M., Bauer, T., Ramunno, L., Vaccari, A., Berini, P., Petrov, Y., Danilov, D., & More Authors (2019). Investigating the Optical Properties of a Laser Induced 3D Self-Assembled Carbon–Metal Hybrid Structure. *Small*, *15*(18), Article 1900512. https://doi.org/10.1002/smll.201900512

# Investigating the Optical Properties of a Laser Induced 3D Self-Assembled Carbon-Metal Hybrid Structure

*Muhammad Abdullah Butt,[1,2,3] Antonino Calà Lesina,[4,5,6,7] Martin Neugebauer,[1,2] Thomas Bauer,[6,8] Lora Ramunno,[4,5] Alessandro Vaccari,[9] Pierre Berini,[4,5,6,7] Yuriy Petrov,[10] Denis Danilov,[11] Alina Manshina,[12] Peter Banzer,[1,2,6,*] and Gerd Leuchs[1,2,4,6]*

*[1]Max Planck Institute for the Science of Light, 91058 Erlangen, Germany*
*[2]Institute of Optics, Information and Photonics, University Erlangen-Nuremberg, 91058 Erlangen, Germany*
*[3]School of Advanced Optical Technologies, University Erlangen-Nuremberg, 91052 Erlangen, Germany*
*[4]Department of Physics, University of Ottawa, Ottawa, ON K1N 6N5, Canada*
*[5]Centre for Research in Photonics, University of Ottawa, Ottawa, ON K1N 6N5, Canada*
*[6]Max Planck - University of Ottawa Centre for Extreme and Quantum Photonics, Ottawa, K1N 6N5, Canada*
*[7]School of Electrical Engineering and Computer Science, University of Ottawa, Ottawa, ON K1N 6N5, Canada*
*[8]Department of Quantum Nanoscience, Delft University of Technology, 2628 CJ Delft, Netherlands*
*[9]Centre for Materials and Microsystems, Fondazione Bruno Kessler, 38123 Trento, Italy*
*[10] Faculty of physics, St. Petersburg State University, St. Petersburg, Russia*
*[11]Interdisciplinary Resource center for Nanotechnology, St. Petersburg State University, St. Petersburg, Russia*
*[12]Institute of Chemistry, St. Petersburg State University, St. Petersburg, Russia*
**peter.banzer@mpl.mpg.de*

Keywords: Orthorhombic carbon, metal alloy nanoparticles, laser-induced deposition, computational modeling, microscopic Müller matrix measurement technique

## Abstract

Carbon-based and carbon-metal hybrid materials hold great potential for applications in optics and electronics. Here, we discuss a novel material made of carbon and gold-silver nanoparticles, fabricated using a laser-induced self-assembly process. This self-assembled metamaterial manifests itself in the form of cuboids with lateral dimensions on the order of several micrometers and a height of tens to hundreds of nanometers. The carbon atoms are arranged following an orthorhombic unit cell, with alloy nanoparticles intercalated in the crystalline carbon matrix. We analyze the optical properties of this metamaterial experimentally using a microscopic Müller matrix measurement approach and reveal a high linear birefringence across the visible spectral range. Theoretical modelling based on local-field theory applied to the

carbon matrix links the birefringence to the orthorhombic unit cell, while finite-difference time-domain simulations of the metamaterial relates the observed optical response to the distribution of the alloy nanoparticles and the optical density of the carbon matrix.

## Introduction

In the last decade, nano-optics has emerged as a scientific field, pushing the boundaries of science. [1] A very important subcategory of this field is the study and fabrication of various 2D and 3D artificial materials, based on layers of structured dielectrics and metals. [2] The reason for the interest in these metamaterials and metasurfaces is the vast variety of applications, such as guiding, shaping and focusing of light beams, the development of ultrathin highly efficient polarizing elements and many more. [3] Recently, orthorhombic carbon phase structures were theoretically predicted, with enhanced optical and structural properties. [4, 5, 6, 7] Carbon allotropes and carbon hybrid materials with embedded metal structures, have been proven to be a beneficial building-block in opto-electronic applications. [8, 9] The combination of carbonaceous materials with metal nanoparticles can give rise to a unique set of properties, which may not be observed in indiviual elements. Fabrication of such structures, has been an active research field with applications ranging from surface enhanced Raman scattering (SERS) to electrochemical processes, enhanced plasmonics response and optical sensing. [10, 11, 12, 13] In recent years, laser induced deposition has been reported as a means for the controllable fabrication of such hybrids. [14, 15] In this process, a laser source is used to trigger a decomposition and transformation of precursor molecules dissolved in a liquid followed by the formation of nanoscale or nanostructured materials. The liquid phase is a solution of a heterometallic supramolecular complex from which the hybrid solid structures are formed. [16, 17]

In this paper, we experimentally and theoretically investigate the optical properties of a novel self-assembled 3D metal-carbon hybrid metamaterial fabricated using a laser-induced deposition process. The metamaterial consists of a carbon phase exhibiting an orthorhombic crystalline matrix intercalated with bimetallic (gold and silver) alloy nanoparticles. [18] The metamaterial self-assembles in the form of cuboids with lateral dimensions on the order of several micrometers and heights of tens to hundreds of nanometers. In the following, we refer to the investigated structures as carbon flakes.

In the next section, we discuss the fabrication and structural details, while in later sections, the complete experimental and numerical analysis of the optical properties of the carbon flakes will be discussed.

## Fabrication of Carbon Flakes

The flakes were synthesized following a laser-induced formation protocol. The experimental scheme is presented in **Figure 1a**. A solution of the supramolecular complex $[Au_{13}Ag_{12}(C_2Ph)_{20}(PPh_2(C_6H_4)_3PPh_2)_3][PF_6]_5$ (hereinafter abbreviated as SMC) in acetophenone (Aldrich, analytically grade purity) at a concentration of 4 mg/ml was placed in a cuvette and covered with a substrate. [19] A microscope cover slip coated with an indium-tin-oxide (ITO) layer was used as the substrate. Laser radiation was directed to the substrate-solution interface from the substrate side without scanning the laser beam. As a light source we used an unfocused He-Cd laser beam (CW, $\lambda = 325$ nm, $I = 0.5$ W/cm$^2$) with the diameter of the laser spot approximately 2 mm. The exposure time to irradiation was 30 min. After the formation process, the substrate was washed with isopropyl alcohol and dried in ambient conditions. The result of the laser-induced deposition process is the formation of rectangular structures with lateral dimensions on the order of several micrometers and a height of tens to hundreds of nanometers (**Figure 1 b**). According to element maps measured with an energy dispersive X-ray spectrometer (**Figure 1c**) the flake contains carbon, gold and silver. **Figure 1d** shows a high-resolution magnified image of an edge of a flake obtained using transmission electron microscopy (TEM). One can see amplitude contrast originating from dense particles embedded in the flake matrix. Selected area electron diffraction (SAED) (**Figure 1e**) shows bright reflexes that correspond to a monocrystalline flake matrix with lattice parameters a=20.8±0.5Å; b=7.99±0.5Å; c=33.4±1Å; α=β=γ=90° corresponding to an orthorhombic crystal system [18] and shown in **Figure 1(f)**, whereas randomly oriented nanoparticles gives a polycrystalline diffuse diffraction ring marked with a grey circle in **Figure 1(e)** with interplanar distance (d) of about 2.35±0.25Å. This is in a good agreement with $d_{111}$=2.36Å that corresponds to the most intense diffraction line for a gold or silver face-centered cubic lattice. [20]

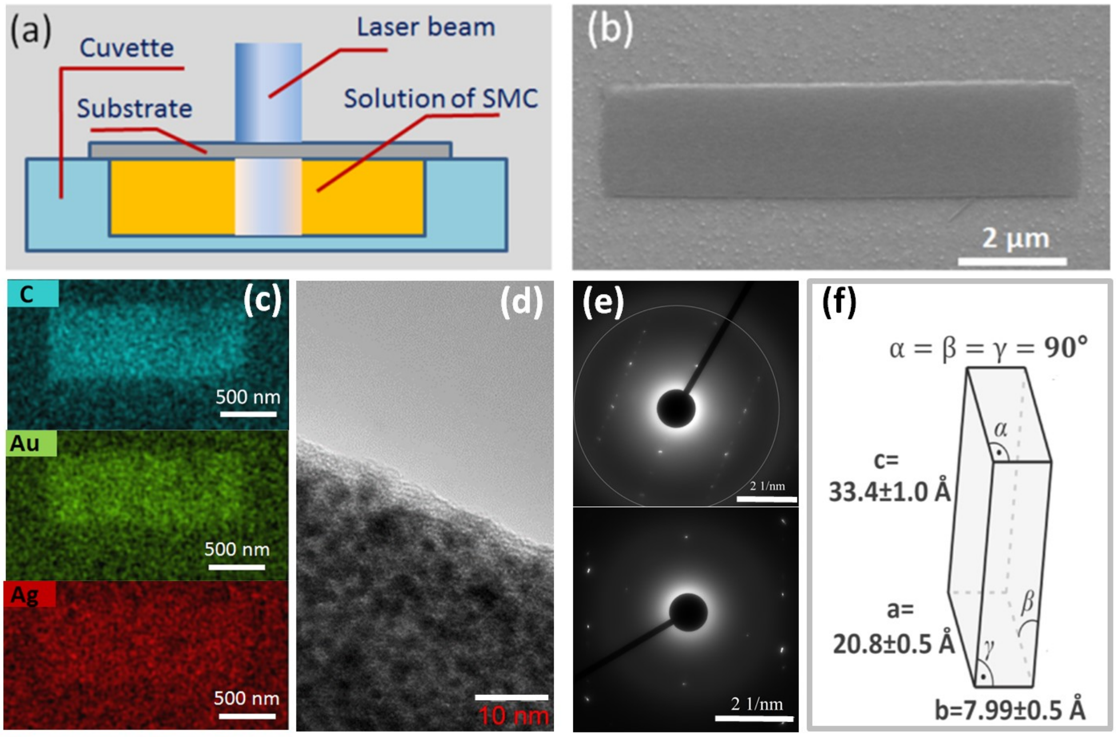

**Figure 1** Formation of the flakes. (a) Scheme of the laser-induced deposition process; (b) typical Scanning Electron Microscope (SEM) image of a fabricated flake. (c) Energy-dispersive X-ray spectroscopy (EDX) mapping of a carbon flake showing presence of carbon (C), gold (Au) and silver (Ag). (d) High-resolution magnified image of an edge of a flake obtained using TEM.(e) Selected area electron diffraction (SAED) obtained from a flake in two different orientations, the diffuse ring corresponding to randomly oriented nanoparticles is marked with a grey circle. (f) Approximate orthorhombic lattice constants calculated using SAED. The lattice constant 'c' is along the thickness/height and 'b' is along the longer lateral dimension of the carbon flake.

It should be pointed out that lattice parameters of gold and silver are very similar, so additional EDX measurements were performed to confirm that the obtained nanoparticles in flakes consist of Au-Ag alloy, rather than being pure gold or silver nanoparticles (see supporting information, **Figure S1**). Summarizing the obtained data, we conclude that such a flake is a unique self-assembled metamaterial, an orthorhombic carbonaceous matrix with inclusions of the bimetallic (Au-Ag) nanoparticles. Owing to its unique structural composition, an experimental investigation of these structures (transferred onto a clean glass substrate) was performed to uncover their optical properties, which will be described in the next section.

## Full Experimental Polarization Analysis of Individual Carbon Flakes - Microscopic Müller Matrix Measurement Technique

In this section, we detail our experimental approach for retrieving the linear optical properties of the individual carbon flakes with lateral dimensions of several square-microns and nanoscale height. Specifically, we quantitatively study linear optical parameters, such as birefringence, attenuation and diattenuation. A sketch of the corresponding experimental setup is depicted in **Figure 2a**. The microscopic Müller matrix measurement technique combines the advantages of back focal plane (k-space) microscopy [21] along with the use of liquid crystal variable retarders (LCVRs) to extract the optical properties of a microscopic structure. The optical measurement technique is based on scanning a focused light beam across the microstructures, which are lying on a glass substrate. [22] To unambiguously retrieve the optical properties of individual flakes using the aforementioned scanning technique, the focused beam must be significantly smaller than the lateral extent of a single flake under study. As a consequence, the effect of edge-induced scattering or coupling can be minimized. A Gaussian beam with a wavelength λ between 400 nm and 700 nm was focused by a microscope objective with an effective numerical aperture (NA) of approximately 0.5, resulting in a FWHM of the spot of about a wavelength. The carbon flake is scanned across the focal spot. For each position, the transmitted light is collected by an oil-immersion microscope objective (NA=1.3) in a large angular range. The back focal plane (BFP) of this collection lens is imaged onto a CCD-camera to get access to the angular spectrum of the transmitted light. [23] In these BFP images, we consider the intensity in the angular range corresponding to near-to-normal incidence only. The effective angular range for data analysis is chosen to be limited by an NA = 0.1, implying a half angle of approximately 5.5° (see white solid circle in **Figure 2b**). In order to test the homogeneity of the investigated carbon flakes, we raster scanned them individually across the beam and measured for each position the transmitted intensity, resulting in the scanning image depicted in **Figure 2c**. The presented data is normalized to the transmission through the bare glass substrate. As it can be seen, the transmission drops drastically when the focused incoming beam is placed on the flake. There, we observe a nearly constant plateau in the center of the flake, implying that edge effects can be neglected for a central placement of the beam. Thus, the averaged polarization parameters of the flake can be determined with statistical significance. To this end, we carefully prepare differently polarized input beams and measure their full Stokes polarization vector after the transmission through the flake. [24] The result is then compared to the transmission through the pure glass substrate next to the flake. The polarization state of the incoming beam was defined by a polarizer mounted in a motorized rotation mount.

The input beam was set to five different linear polarization states between 0° and 180° in steps of 45°. Additionally, a left- and right-hand circularly polarized beam was prepared using a zero-order quarter-wave plate. After the transmission of the beam through the flake (or the bare glass substrate for normalization purposes), we measure the Stokes parameters of the transmitted light. For that purpose, we use electrically tunable liquid crystal variable retarders (LCVRs) followed by a fixed polarization analyzer (Glan Taylor prism). [25] Aligning the slow axis of the LCVRs cells under 22.5° and 45° with respect to the chosen coordinate frame allows for measuring the full Stokes vector by switching between zero, half-wave and quarter-wave retardance. Calibration of the LCVRs for different wavelengths, was carried out before the experimental scan measurements [26].

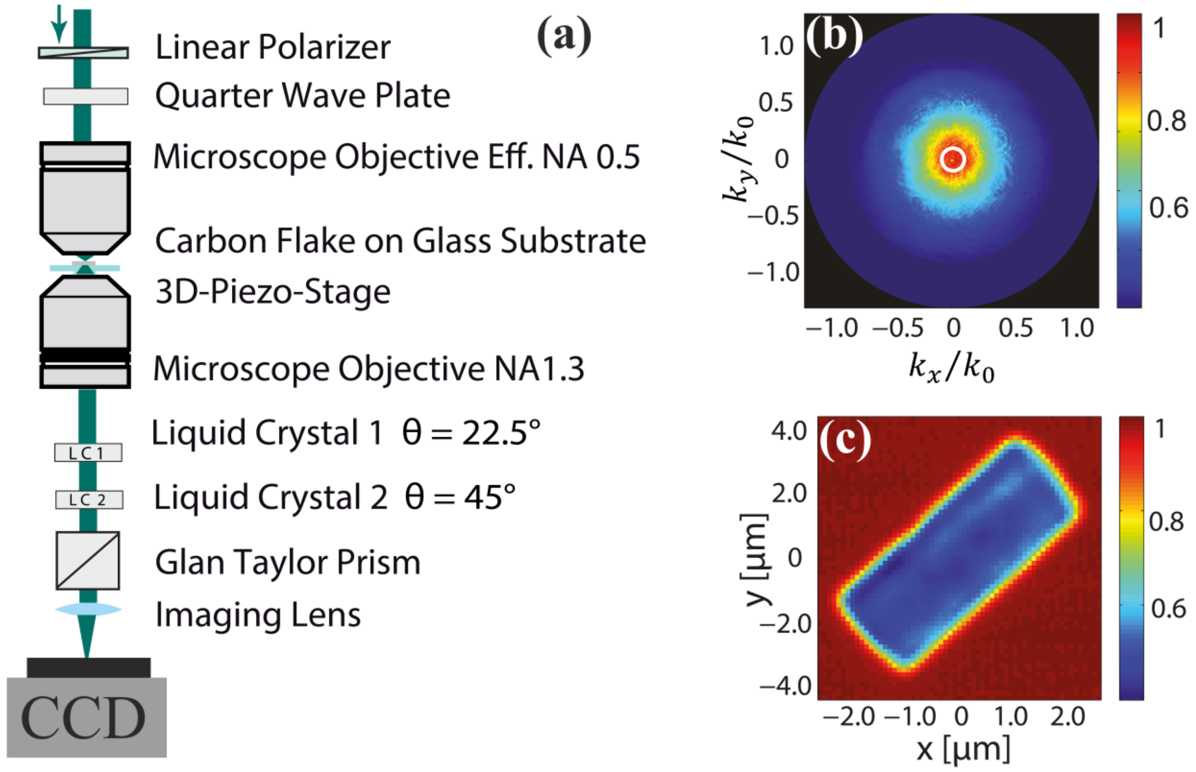

**Figure 2** The experimental setup for Müller matrix polarimetry of individual carbon flakes. (a) Simplified sketch of the experimental setup. The combination of a polarizer and a zero-order quarter -wave plate defines the incident polarization states. The light beam is then focused by a 0.9 NA objective (effective NA approximately 0.5) onto the carbon flake present on a glass substrate. The sample is raster scanned through the beam by a piezo stage. The transmitted light is collected by an objective of 1.3 NA. The polarization analysis is performed by two LCVRs and a Glan Taylor prism as a fixed polarization analyzer. The LCVRs are oriented along 22.5° and 45° relative to their slow axis, to project onto six polarization states required for a complete Stokes parameter analysis. Thereafter, the polarization-filtered BFP intensity distribution of the collection microscope objective is imaged onto a CCD camera. (b) Example image of the BFP of the collection microscope objective on the glass substrate, for a wavelength $\lambda = 460$ nm. The solid white line shows the utilized maximum collection angle defined by NA = 0.1. (c) Scan image of the transmitted optical intensity when scanning the carbon flake through the focal field distribution. The sharp edges of the flake show the precise orientation with respect to the experimental coordinate system. The plateau at the center of the flake indicates the homogeneity of the material and the proper choice of the input beam size with respect to the flake dimensions.

The use of LCVRs ensure that there is no moving optical element in the polarization analysis part of the setup. This helps in avoiding rotation induced shift of the BFP image, which can give rise to cross-talk of polarization information in different adjacent k-vectors of the beam. This procedure is performed for various positions of the beam relative to the flake (several positions in the plateau region on the flake and several reference measurements on glass).

### Retrieval of the Müller matrix

As stated above, to retrieve the Müller matrix of individual carbon flakes from our experiments, several measurements of the transmitted Stokes vector for differently polarized input beams (here we use a set of seven input polarization states) are required. [27, 28] All intensity values collected for the different settings of the LCVR and for the different positions of the beam relative to the carbon flake were normalized to a reference intensity measured at the output of the laser in order to decrease the influence of intensity fluctuations of the laser. To account for a non-perfect polarization selection of the LC cells, the Müller matrix of the analysis system was determined separately by a measurement of several different known input polarizations. From the transmission of the input beam through the bare glass substrate and carbon flakes, the Stokes parameters $\hat{S}_{in}$ and $\hat{S}_{out}$ of the different input beams are retrieved respectively. This allows us to use the 4 x 7 matrix of the input and output Stokes vectors, obtained by combining the values for all measured beams, to determine the Müller matrix. [29, 30, 21, 31] Since the system of linear equations is overdetermined, we can calculate the Müller matrix $\widehat{M}$ with the help of the pseudo-inverse input Stokes vector ${S_{in}}^{+}$: [32]

$$\hat{S}_{out} = \widehat{M}\hat{S}_{in}, \tag{1}$$

$$\widehat{M} = \hat{S}_{out}.{S_{in}}^{+} = S_{out}.\left({S_{in}}^{\dagger}S_{in}\right)^{-1}{S_{in}}^{\dagger}. \tag{2}$$

Finally, the experimentally measured Müller matrix can be used to retrieve optical properties such as attenuation, birefringence and diattenuation by Müller matrix decomposition techniques. [27, 28, 29, 31]

### Experimental Results and Analysis

An example of two-dimensional raster scan images (41 × 21 steps with a step-size of 200 nm × 270 nm) measured at λ = 460 nm and corresponding to the attenuation (calculated as 1-normalized transmission intensity), diattenuation, orientation of the optic axis of a flake, and birefringence are shown in **Figures 3a-3d** respectively. The attenuation (A) is fairly strong and constant across the central region of the flake. The diattenuation (D) is found to be negligible across the flake except at the edges, where it can be naturally assumed to be high due to edge effects. For the sake of brevity, the diattenuation will not be further discussed in the remaining part of the paper. The fast axis orientation of the carbon flake corresponds very well to its geometrical structure, with the axis being parallel to the long side of the flake. The optical birefringence Δn, is calculated from the retardance using the relation:

$$\text{Birefringence} = \Delta n = \frac{\delta\lambda}{2\pi t}, \qquad (3)$$

where the thickness/height '$t$' of the flake is defined by using atomic force microscopy (AFM), $\delta$ is the retardance calculated by the Müller matrix decomposition and $\lambda$ the wavelength of the light beam.

As it can be seen, a high linear optical birefringence occurs also in the central region of the flake where edge effects can be neglected (**Figure 3d**). This indicates that the birefringence is a property of the hybrid material itself and not of its shape or edges. In particular, the birefringence is apparently linked to the orthorhombic crystalline structure of the carbon matrix. In order to further investigate the birefringence, we perform a detailed spectral analysis in the visible spectrum.

For individual wavelengths, a mean value for each of the extracted optical properties was calculated based on the data points from the center of the flake. To study the spectral behavior of the attenuation A and linear birefringence Δn, the excitation wavelength $\lambda$ was tuned from 400 nm to 700 nm in steps of 20 nm and additionally to a few other wavelengths. As a result, we plot the spectral dependence of the attenuation and birefringence in **Figures 3e** and 3**f**. The attenuation of the carbon flake increases at shorter wavelengths with a maximum around $\lambda = 460$ nm. Interestingly, the birefringence is found to be approximately constant (~0.09 ±0.005**)** across the entire spectral range investigated.

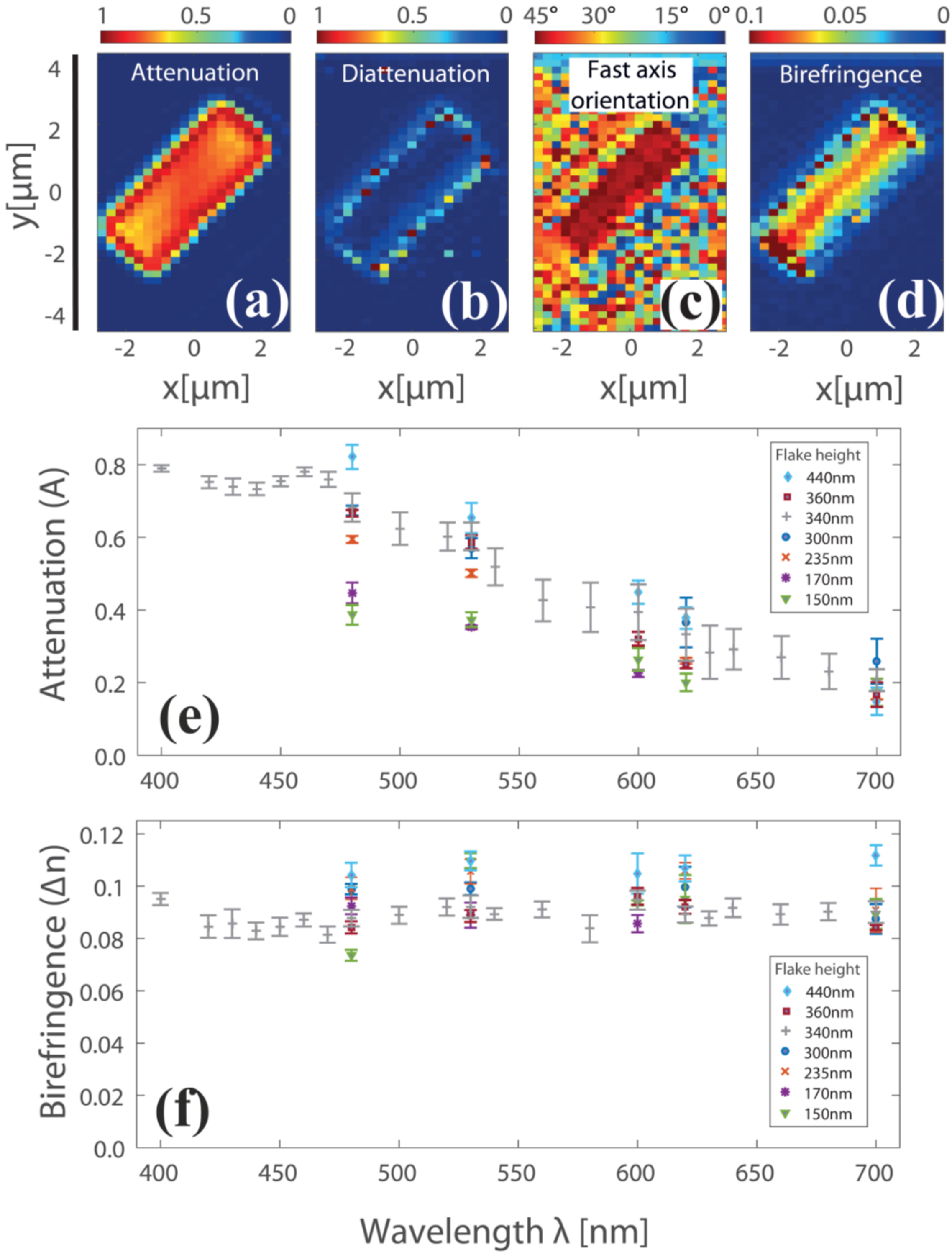

**Figure 3** Experimental results. (a-d) Two-dimensional raster scans of a flake of dimensions 5.2 µm x 2 µm x 340 nm at λ = 460 nm, showing attenuation, diattenuation, fast axis orientation, and birefringence. The scans were performed as 41 x 21 steps using a 200 nm step size. (e & f) Spectral analysis of attenuation and birefringence for multiple flakes of different heights and lateral dimensions (of at least few microns to avoid edge effects at all wavelengths). The attenuation increases at shorter wavelengths, whereas the birefringence remains high and nearly constant throughout the visible range.

To verify the high birefringence of the material, multiple flakes of different thicknesses and lateral dimensions (of at least a few microns to avoid edge effects) were investigated. The analysis of those additional flakes was performed at fewer wavelengths but using the same measurement and analysis techniques. AFM measurements were also performed to estimate the height of each carbon flake under study. Remarkably, all investigated flakes show comparable values of birefringence (see colored data points in **Figure 3f**).

## Theoretical Model

To theoretically model the optical properties of the carbon flakes, we consider two contributions, to the overall optical response: Au-Ag alloy nanoparticles and the carbon matrix. Detailed analysis with a TEM revealed that the average radius of the metallic nanoparticles is $d$ =2R=2.5±0.9 nm, with center-to-center interdistance of $D_{cc}$=7.3±1.5 nm. A crystallographic analysis reveals that the arrangement of the carbon atoms follows an orthorhombic lattice, with lattice parameters as mentioned in the fabrication section of this article. The fact that the diameter of nanoparticle (2R) is comparable to $c$, suggests that the Au-Ag nanoparticles are intercalated in the carbon matrix as depicted in **Figure 4**, where we model the latter as graphene-like sheets for illustrative purposes. It is important to note here, that the use of graphene-like sheets acts only as a starting point for our theoretical model. Subsequently, different modifications will be applied to adapt the theoretically modelled system to the real flakes and their configuration.

Inspired by the experimental data for the flake with height 340 nm, we built the computational model by distributing alloy nanoparticles in a carbon matrix of thickness t= 340 nm (along the $z$-axis). The carbon matrix is composed of carbon sheets arranged along $z$, separated by distance $c$= 3.34 nm, as sketched in **Figure 4**. Experimental structural analysis suggests that carbon atoms are present also in the space between the carbon sheets. Thus, we model the background material of thickness '*t*' with a constant refractive index $n_{back} \geq 1$. The bimetallic nanospheres of radius $R$=1.25 nm are arranged in the carbon matrix in a face-centered cubic (FCC) fashion, and the (1,1,1) FCC planes of nanoparticles are aligned along the *z*-axis (out-of-plane) with a distance between planes of $c$=3.34 nm. FCC is preferred because it is the most closely packed lattice, and this choice is inspired by the distribution of the bimetallic nanoparticles in TEM images.

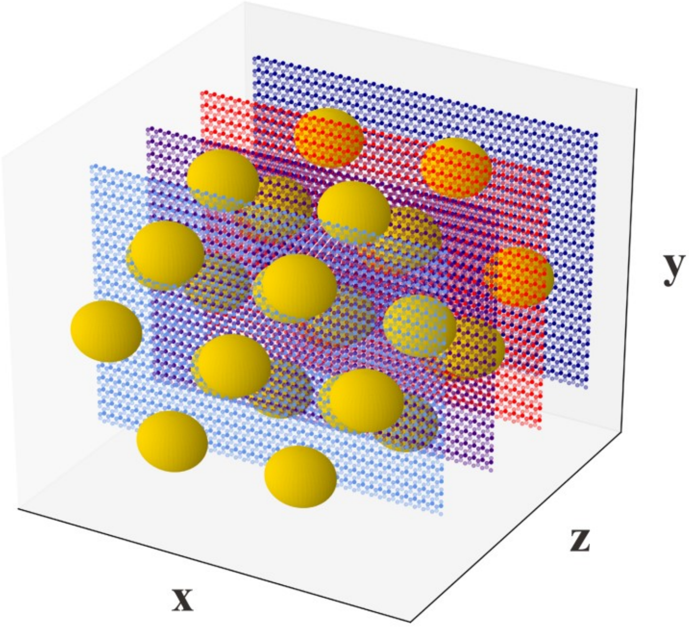

**Figure 4** Carbon sheets (graphene-like) intercalated with metal nanoparticles

The in-plane interdistance (*i.e.* along *xy*), between the nanoparticles is $D_{cc}$ (centre-to-centre). The number of nanoparticles FCC planes and carbon sheets needed to simulate the full flake thickness '*t*' is 102. The model in **Figure 4** was simulated by using a finite-difference time-domain (FDTD) in-house software on the IBM BlueGene/Q operated by SOSCIP, Canada. [33] In the model, light propagates along the *z*-direction, is *y*-polarized, and periodic boundary conditions (PBCs) are applied along *x* and *y*. [34] A uniform space-step of $dx$= 0.05 nm was used to discretize the simulation domain and guarantee the accuracy and convergence of the results. For the nanoparticles, we consider an alloy with an equal amount of gold and silver based on the composition of the carbon flake analyzed using the EDX mapping spectroscopy. The complex refractive index of the $Au_{0.5}$-$Ag_{0.5}$ alloy [35] is fitted to a Drude model with $N_{CP}$=2 critical points: [36]

$$\chi(\omega) = \chi_{\mathrm{Drude}}(\omega) + \sum_{p=1}^{N_{CP}} \chi_{CP}^{(p)}(\omega) = \frac{-\omega_D^2}{\omega(\omega+i\gamma)} + \sum_{p=1}^{N_{CP}} A_p\, \Omega_p \left(\frac{e^{i\phi_p}}{\Omega_p-\omega-i\Gamma_p} + \frac{e^{-i\phi_p}}{\Omega_p+\omega+i\Gamma_p}\right), \tag{4}$$

with parameters $\varepsilon_\infty$= 2.0754, $\omega_D$= 1.3709 x $10^{16}$ rad/s, $\gamma$= 2.5469 x $10^{14}$ rad/s, $\Omega_1$= 5.3683 x $10^{15}$ rad/s, $\Omega_2$= 4.407 x $10^{15}$ rad/s, $\Gamma_1$= 2.6119 x $10^{15}$ rad/s, $\Gamma_2$= 8.2708 x $10^{14}$ rad/s, $A_1$= 1.9252, $A_2$= 0.2436, $\phi_1$= -0.5849 rad, $\phi_2$= -1.972 rad, valid in the range 270–1200 nm.

The carbon sheets are modelled by “stretching” the permittivity of graphene in *x* and *y* direction. A graphene sheet can be simulated in FDTD by applying its complex permittivity [37] to a one-atom-thick carbon layer (the van der Waals diameter of a carbon atom is $d_W^{(C)}$= 3.4 Å) along *x* and *y*, while using the vacuum permittivity in *z*. The permittivity of graphene was fitted in the range 270-1000 nm to a Drude model with $N_{CP}$= 4 critical points, *i.e.*,

$$\varepsilon_{graphene}(\omega) = \varepsilon_\infty + \chi_{\mathrm{graphene}}(\omega) = \varepsilon_\infty + \chi_{Drude}(\omega) + \sum_{p=1}^{4} \chi_{CP}^{(p)}(\omega), \tag{5}$$

obtaining $\varepsilon_\infty$= 1, $\omega_D$= 5.2796 x $10^{15}$ rad/s, $\gamma$= 9 x $10^{15}$ rad/s, $\Omega_1$= 6.1264 x $10^{14}$ rad/s, $\Omega_2$= 6.6843 x $10^{15}$ rad/s, $\Omega_3$= 5.6289 x $10^{15}$ rad/s, $\Omega_4$= 1.118 x $10^{16}$ rad/s, $\Gamma_1$= 1 x $10^{14}$ rad/s, $\Gamma_2$= 7.9051 x $10^{14}$ rad/s, $\Gamma_3$= 6.7526 x $10^{14}$ rad/s, $\Gamma_4$= 1.0005 x $10^{14}$ rad/s, $A_1$= 13.1068, $A_2$= 1.8417, $A_3$= 0.4191, $A_4$= 0.7737, $\phi_1$= -1.8391 rad, $\phi_2$= 0.3505 rad, $\phi_3$= 3.0565 rad, $\phi_4$= -0.1199 rad. The carbon sheets are modelled as one-cell thick (*dx*= 0.05 nm) layers, whose permittivity is

$$\varepsilon_{zz}(\omega) = n_{back}^2 \text{ and} \tag{6}$$

$$\varepsilon_{xx}(\omega) = \varepsilon_{yy}(\omega) = 1 + f * s * \chi_{graphene}(\omega), \tag{7}$$

where $s= d_W^{(C)}/dx$ is a scaling factor between van der Waals diameter and *dx*, and *f* is a fitting parameter (*f* < 1) caracterizing the amount of stretching applied to graphene, where f=1 defines unstretched. To compare simulation results with experimental measurements, we calculated the attenuation as 1 - transmittance.

A parametric study on $D_{cc}$, *R*, *f*, alloy composition, and $n_{back}$ is shown in **Figure 5**. Starting from the red curve obtained for $D_{cc}$= 8 nm, *f*= 0.1, $n_{back}$= 1.2, *R*= 1.25 nm and $Au_{0.5}$-$Ag_{0.5}$, we modify each parameter to understand how it influences the attenuation of the system. We consider the following values: $D_{cc}$= {6, 8, 10} nm in **Figure 5(a)**, $R$= {1, 1.25, 1.5} nm in **Figure 5(b)**, $f$ = {0.05, 0.1, 0.15} in **Figure 5(c)**, Au-Ag composition= {$Au_{0.0}$-$Ag_{1.0}$, $Au_{0.4}$-$Ag_{0.6}$, $Au_{0.5}$-$Ag_{0.5}$, $Au_{0.6}$-$Ag_{0.4}$, $Au_{1.0}$-$Ag_{0.0}$} in **Figure 5(d)**, $n_{back}$= {1, 1.2, 1.4} in **Figure 5(e)**, and $n_{back}$= {1.2, 1.3, 1.4} for $D_{cc}$= 10 nm in **Figure 5(f)**. In the same figure, we also show the measured attenuation (average value and standard deviation - black points) for a carbon flake of thickness t= 340 nm. In **Figures 5(a)** and **5(b)**, we show that the level of the attenuation increases by decreasing $D_{cc}$ and by increasing $R$. This dependence becomes weaker for increasing wavelength. In **Figure 5(c)**, we show that the level of the attenuation increases by increasing $f$, and this dependence becomes stronger at longer wavelengths. In **Figure 5(d)**, we observe a red-shift in the plasmonic resonance for an increasing percentage of Au in the Au-Ag alloy. In **Figure 5(e)**, we show that the level of the attenuation increases by increasing $n_{back}$. We also observe a red-shift in the plasmonic resonance for increasing $n_{back}$. In **Figure 5(f)**, the reference simulation considers $D_{cc}$= 10 nm, we observe the same trend in the attenuation for increasing $n_{back}$.

In general, the attenuation at longer wavelengths is mostly affected by $f$ and $n_{back}$.variations, while the attenuation at shorter wavelengths is mostly due to $D_{cc}$, $R$, $n_{back}$ and alloy composition variations. Finding the right combination of parameters to match exactly the experimental curves is not trivial. Throughout our parameteric investigation, we found that we can match the plasmonic resonance by changing $n_{back}$. and the alloy composition, and we have identified two combinations matching the plasmonic resonance reported in the experimental measurements at $\lambda_0$= 460 nm : the green curve for $Au_{0.6}$-$Ag_{0.4}$ in **Figure 5(d)** and the green curve for $n_{back}$= 1.4 in **Figure 5(f)**. This simulation study provides a valuable guideline to understand the internal composition of the metamaterial.

Despite the simulated attenuation, which shows one peak in the investigated spectral range, in the experimental data also shown in **Figure 5** we notice peaks at wavelengths of 460 nm, 520 nm, 600 nm, and a peak for $\lambda_0 < 400$ nm. These resonances could be explained by considering nanoparticles made entirely by gold or silver (see the curve for $Au_{1.0}$-$Ag_{0.0}$ and $Au_{0.0}$-$Ag_{1.0}$), or other compositions for the alloy.

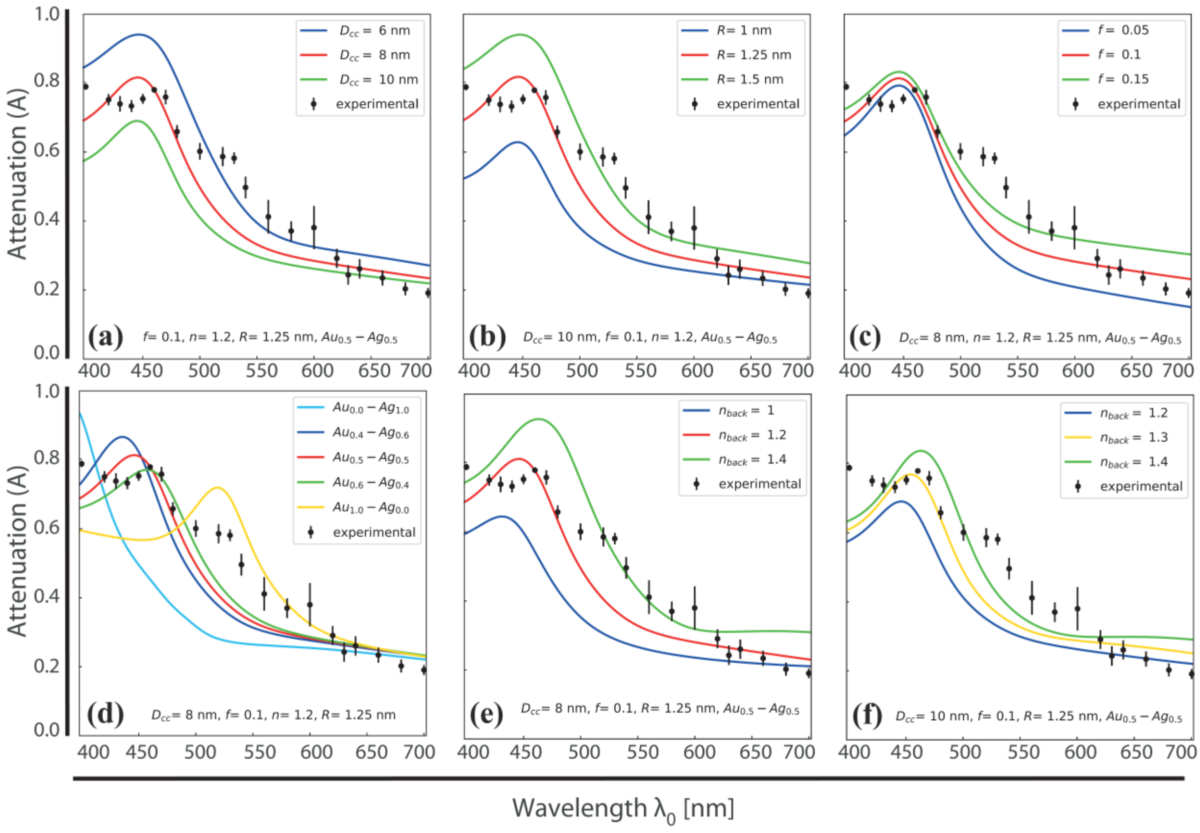

**Figure 5** Parametric study ($D_{cc}$, $R$, $f$, alloy percentage, and $n_{back}$ variation).

The long wavelength peak at 600 nm could also be due to the presence of bigger nanoparticles, nanoparticles with a shell, or a local variation of the effective refractive index within the carbon flake. In **Media 1** and **Media 2** (in the supporting information), we show the evolution of the electric field as a plane-wave pulse interacts with the carbon flake model in a representative case ($D_{cc}$= 10 nm, $n_{back}$= 1, $R$= 1.45, $Au_{0.5}$-$Ag_{0.5}$, 30 layers with distance between carbon sheets of 3.09 nm) for $f$ = 0.1 and $f$ = 0.8, respectively. By comparing the two cases, we can clearly see the effect of the carbon sheets, for $f$ = 0.8, which create a field confinement around the nanoparticles, and are responsible for the higher attenuation shown in **Figure 5(c)** for increasing $f$.

The arrangement of the bimetallic nanoparticles and the carbon matrix model cannot explain the birefringence of the metamaterial. The birefringence is explained by expanding the local-field theory for a cubic lattice [38, 39, 40] to the case of an orthorhombic lattice with a unit cell of sizes $a$, $b$ and $c$, [41] with a number $n_C$ of carbon atoms randomly distributed in the unit cell. In this case, we obtain three different values for the diagonal components of the susceptibility tensor of the carbon lattice:

$$\chi_{xx} = \frac{N\alpha}{1-\frac{\alpha n_C}{4\pi}F_{xx}-\frac{N\alpha}{3}}, \chi_{yy} = \frac{N\alpha}{1-\frac{\alpha n_C}{4\pi}F_{yy}-\frac{N\alpha}{3}}, \chi_{zz} = \frac{N\alpha}{1-\frac{\alpha n_C}{4\pi}F_{zz}-\frac{N\alpha}{3}}, \qquad (8)$$

where α is the isotropic static polarizability of the carbon atom (2.38 Å$^3$), [42] $N = n_C / (a \cdot b \cdot c)$ is the atomic density, and $F_{xx}$= -0.003565, $F_{yy}$= 0.008672 and $F_{zz}$= -0.005107 are the elements of the local-field tensor, with $F_{xx} + F_{yy} + F_{zz} = 0$. For the case of a cubic lattice with one atom per unit cell, we would have $F_{xx} = F_{yy} = F_{zz} = 0$, which leads to the well-known Clausius-Mossotti formula $\chi = N\alpha / (1 - N\alpha/3)$.

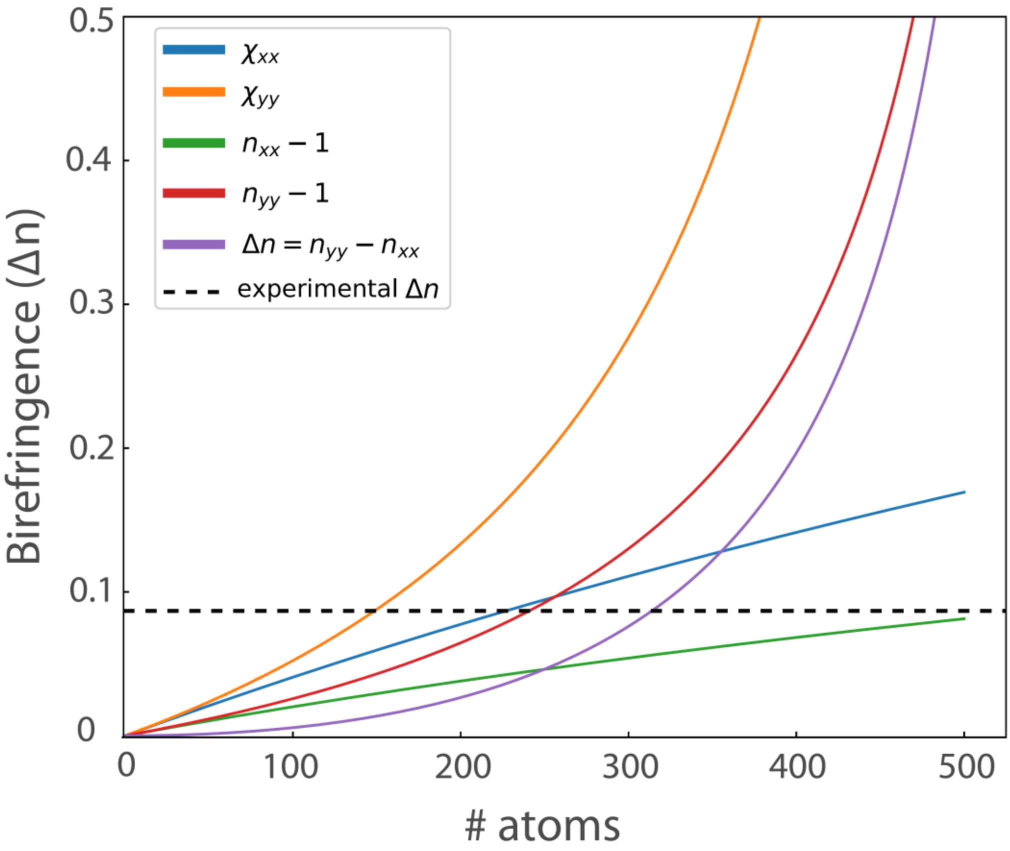

**Figure 6** Orthorhombic lattice – susceptibility and birefringence vs. number of carbon atoms

In **Figure 6**, we show the susceptibility tensor elements and the birefringence, defined as $n_{yy}$ - $n_{xx}$, obtained through our theoretical model as a function of the number of carbon atoms $n_C$ in the orthorhombic unit cell. In this case, to match the birefringence of ~0.09 reported in experiments we need a number of carbon atoms around 300. This number of carbon atoms is of the same order of magnitude as what we can estimate by knowing the average size measurements, the inter-distance between nanoparticles, and the percentage of metal and carbon atoms in the metamaterial, which is approximately 93% carbon, 7% metal, according to X-ray photo-electron spectroscopy (XPS). The exact arrangement and number of carbon atoms in the orthorhombic unit cell is still unknown and is currently under investigation.

## Conclusion

We discuss the fabrication, experimental investigation and numerical analysis of laser induced self-assembled 3D carbon structures, with Au-Ag nanoparticles embedded in it (carbon flakes). Our studies show that this novel hybrid metamaterial features a linear birefringence mainly caused by the orthorhombic carbon phase. The linear birefringence remains nearly constant ($\Delta n=0.09 \pm 0.005$) over a spectral range of 400–700 nm, which is generally comparable to naturally birefringent materials, but it outperforms other orthorhombic crystalline structures. [43] Furthermore, the combination of the field enhancement introduced by the plasmonic Au-Ag nanoparticle inclusions and the birefringence suggest a strong potential for opto-electronics, nanophotonic, nonlinear optical experiments and applications. [13, 14]

## Acknowledgements

TEM and SAED data were obtained using equipment of Interdisciplinary Resource Center for Nanotechnology of St. Petersburg State University. This work was supported by the RFBR grant #17-03-01284, and St.Petersburg state university grant for equipment #12.40.1342.2017.

The authors acknowledge the Canada Research Chairs program, the Southern Ontario Smart Computing Innovation Platform (SOSCIP), and SciNet. This work was further supported by the German Research Foundation (Deutsche Forschungsgemeinschaft, DFG) by funding the Erlangen Graduate School in Advanced Optical Technologies (SAOT) within the German Excellence Initiative.

**References**

[1] L. Novotny and B. Hecht, Principles of NanoOptics, Cambridge University Press, **2006**.

[2] D. Jariwala, T. J. Marks, M. C. Hersam, *Nat. Mater.* **2017**, https://doi.org/10.1038/nmat4703

[3] G. R. Bhimanapati, L. Zhong, V. Meunier, Y. Jung, J. Cha, S. Das, D. Xiao, Y. Son, M. S. Strano, V. R. Cooper, L. Liang, S. G. Louie, E. Ringe, W. Zhou, S. S. Kim, R. R. Naik, B. G. Sumpter, H. Terrones, F. Xia, Y. Wang, J. Zhu, D. Akinwande, N. Alem, J. A. Schuller, R. E. Schaak, M. Terrones, J. A. Robinson, *ACS Nano* **2015**, https://doi.org/10.1021/acsnano.5b05556.

[4] Z.-Z. Li, J.-T. Wang, H. Mizuseki, C. Chen, *Phys. Rev. B* **2018**, https://doi.org/10.1103/PhysRevB.98.094107

[5] Q. Weia, C. Zhao, M. Zhang, H. Yand, Y. Zhoua, R. Yaoa, *Phys. Lett. A* **2018**, https://doi.org/10.1016/j.physleta.2018.04.024.

[6] Z.-Z. Li and J.-T. Wang, *RSC Phys. Chem. Chem. Phys.* **2018**, https://doi.org/10.1039/C8CP04129F

[7] Z.-Z. Li, J. Chen, S. Nie, L. Xu, H. Mizusekie, H. Weng, J.-T. Wang, *Carbon* **2018**, https://doi.org/10.1016/j.carbon.2018.03.003.

[8] D. Jariwala, V. sangwan, L. Lauhon, T. Marks, M. Hersam, *Chem. Soc. Rev.* **2013**, https://doi.org/10.1039/c2cs35335k.

[9] S. Z. Butler, S. M. Hollen, L. Cao, Y. Cui, J. A. Gupta, H. R. Gutiérrez, T. F. Heinz, S. S. Hong, J. Huang, A. F. Ismach, E. Johnston-Halperin, M. Kuno, V. V. Plashnitsa, R. D. Robinson, R. S. Ruoff, S. Salahuddin, J. Shan, L. Shi, M. G. Spencer, M. Terrones, W. Windl, J. E. Goldberger, *ACS Nano* **2013**, https://doi.org/10.1021/nn400280c.

[10] C. Tan, X. Huang, H. Zhang, *Mater. Today* **2013**, https://doi.org/10.1002/10.1016/j.mattod.2013.01.021.

[11] A. Baron, A. Aradian, V. Ponsinet, P. Barois, *Opt. Laser Technol.* **2016**, https://doi.org/10.1016/j.optlastec.2016.02.024.

[12] S. Schlicht, A. Kireev, A. Vasileva, E. V. Grachova, S. P. Tunik , A. A. Manshina, J. Bachmann, *Nanotechnology* **2017**, https://doi.org/10.1088/1361-6528/aa536a

[13] M. Bashouti, A. Manshina , A. Povolotckaia, A. Povolotskiy , A. Kireev , Y. Petrov, M. Mačković , E. Spiecker , I. Koshevoy, S. Tunik, S. Christiansen , *Lab Chip* **2015**, https://doi.org/10.1039/c4lc01376j.

[14] A. Povolotskiy, A. Povolotckaia, Y. Petrov, A. Manshina, S. Tunik, *Appl. Phys. Lett.* *2***013**, https://doi.org/10.1063/1.4820841.

[15] A. A. Manshina, E. V. Grachova, . A. V. Povolotskiy, A. V. Povolotckaia, Y. V. Petrov , I. O. Koshevoy, A. A. Makarova , D. V. Vyalikh, S. P. Tunik , *Sci Rep.* **2015**, https://doi.org/10.1038/srep12027.

[16] M. Y. Bashouti, A. V. Povolotckaia, . A. V. Povolotskiy, S. P. Tunik, S. H. Christ, G. Leuchs, A. A. Manshina, *RSC Adv.* **2016***,* https://doi.org/10.1039/C6RA16585K.

[17] A. Povolotskaya, A. Povolotskiy, A. Manshina, *Russ. Chem. Rev.* **2015**, https://doi.org/10.1070/RCR4487

[18] A. Povolotckaia, D. Pankin, Y. Petrov, A. Vasileva, I. Kolesnikov, G. Sarau, S. Christiansen, G. Leuchs, A. Manshina, *J. Mater. Sci* **2019**, https://doi.org/ 10.1007/s10853-019-03478-9.

[19] I. O. Koshevoy, A. J. Karttunen, S. P. Tunik, . M. Haukka, S. I. Selivanov, A. S. Melnikov, P. Y. Serdobintsev, T. A. Pakkanen, *Organometallics* **2009**, https://doi.org/10.1021/om8010036.

[20] R. Wyckoff, Crystal Structures, New York: Interscience Publishers, **1963**.

[21] O. Arteaga, M. Baldrís, J. Antó, A. Canillas, E. Pascual, E. Bertran, *Appl. Opt.* **2014**, https://doi.org/10.1364/AO.53.002236.

[22] P. Banzer, U. Peschel, S. Quabis, G. Leuchs, *Opt. Express* **2010**, https://doi.org/10.1364/OE.18.010905.

[23] O. Arteaga, S. M. Nichols, J. Antó, *Appl. Surf. Sci.* **2017**, https://doi.org/10.1016/j.apsusc.2016.10.129.

[24] G. G. Stokes, *Trans. Cambridge Philos. Soc.* **1852**, https://doi.org/10.1017/CBO9780511702266.010.

[25] S. T. Wu, U. Efron, L. D. Hess *Appl. Opt.* **1984**, https://doi.org/10.1364/AO.23.003911.

[26] J. M. Bueno, *J. Opt. A: Pure Appl. Opt.* **2000**, https://doi.org/10.1364/AO.46.000689.

[27] R. Azzam, *J. Opt. Soc. Am.* **2016**, https://doi.org/10.1364/JOSAA.33.001396.

[28] M. Bass, C. DeCusatis, J. Enoch, V. Lakshminarayanan, G. Li, C. Macdonald, V. Mahajan, E. V. Stryland, *Handbook of Optics Volume II: Design, Fabrication and Testing, Sources and Detectors, Radiometry and Photometry*, McGraw-Hill, New York, USA, **2010**.

[29] S.-Y. Lu, R. A. Chipman, *J. Opt. Soc. Am. A* **1996**, https://doi.org/10.1364/JOSAA.13.001106.

[30] H. D. Noble, R. A. Chipman, *Opt. Express* **2012**, https://doi.org/10.1364/OE.20.000017.

[31] O. Arteaga, A. Canillas, *Opt. Lett.* **2010**, https://doi.org/10.1364/OL.35.000559.

[32] M. Bass, C. DeCusatis, J. Enoch, V. Lakshminarayanan, G. Li, C. Macdonald, V. Mahajan, E. V. Stryland, *Handbook of Optics Volume I. Geometrical and Physical Optics, Polarized Light, Components and Instruments*, McGraw-Hill, New York, USA , **2010**.

[33] A. Calà Lesina, A. Vaccari, P. Berini, L. Ramunno, *Opt. Express* **2015** *,* https://doi.org/10.1364/OE.23.010481.

[34] A. Vaccari, A. Calà Lesina, L. Cristoforetti, A. Chiappini, L. Crema, L. Calliari, L. Ramunno, P. Berini, M. Ferrari, *Opt. Express* **2014**, https://doi.org/10.1364/OE.22.027739.

[35] D. Rioux, S. Vallières, S. Besner, P. Muñoz, E. Mazur, M. Meunier, *Adv. Opt. Mater.* **2014**, https://doi.org/10.1002/adom.201300457.

[36] A. Vial, T. Laroche, M. Dridi, L. Le Cunff, *Appl. Phys. A : Mater. Sci. and Process.* **2011**, https://doi.org/10.1007/s00339-010-6224-9.

[37] J. W. Weber, V. E. Calado, M. C. M. van de Sanden, *Appl. Phys. Lett.* **2010**, https://doi.org/10.1063/1.3475393.

[38] D. E. Aspnes, *Am. J. Phys.* **1982**, https://doi.org/10.1119/1.12734.

[39] B. Nijboer, F. D. Wette, *Physica,* **1957**, https://doi.org/10.1016/S0031-8914(57)92124-9.

[40] B. Nijboer, F. D. Wette, *Physica* **1958**, https://doi.org/10.1016/S0031-8914(58)95803-8.

[41] C. K. Purvis, P. L. Taylor, *Phys. Rev. B* **1982**, https://doi.org/10.1103/PhysRevB.26.4547

[42] J. H. Miller, H. P. Kelly, *Phys. Rev. [Sect.] A* **1972**, https://doi.org/10.1103/PhysRevA.5.516

[43] Z. L. Gao, Q. Wu, X. T. Liu, Y. X. Sun, X. T. Tao, *Opt. Express* **2015**, https://doi.org/10.1364/OE.23.003851.